Droplet Misalignment Limit for Inkjet Printing into Cavities on Textured Surfaces

Frankie F. Jackson[1,*], Krzysztof J. Kubiak[1,*], Mark C. T. Wilson[1], Marco Molinari[2], Viacheslav Stetsyuk[3]

[1]University of Leeds, School of Mechanical Engineering, Leeds LS2 9JT, United Kingdom
[2]University of Huddersfield, Department of Chemistry, School of Applied Sciences, Huddersfield HD1 3DH, United Kingdom
[3]University of Huddersfield, Department of Engineering and Technology, School of Computing and Engineering, Huddersfield HD1 3DH, United Kingdom

Keywords: Additive manufacturing, lattice Boltzmann method, OLED, inkjet printing, functional surface, square cavities.

Abstract

The control of droplets deposited onto textured surfaces is of great importance for both engineering and medical applications. This research investigates the dynamics of a single droplet deposited into a confined space and its final equilibrium morphology, with emphasis given to droplet deposition under print-head misalignment, the effect of non-uniform wettability, and deposition of varying size droplets. A multi-phase pseudopotential lattice Boltzmann methodology is used to simulate the process of deposition. The print quality is characterized in terms of a parameter referred to as the wetted fraction (*WF*), which describes the proportion of the cavity which is wetted by the droplet. Our results show how single and multiple axis misalignment affects the final equilibrium morphology, and it was found for comparable configurations that multi-axis misalignment resulted in a higher wetted fraction. Investigations into wettabilities of the substrate and cavity wall revealed how larger ratios of the contact angles between the two enhance the ability for the droplet to self-align within the cavity. Additionally, a range of uniform wettabilities between the substrate and cavity were found which mitigate against misalignment. Investigations into varying droplet size relative to the cavity revealed how misalignment can be compensated for with larger droplets, and an upper limit is defined such that the droplet does not overflow. Finally, we explore the deposition with misalignment into closely positioned cavities where it is found that the spacing between cavities is a key factor in determining the maximum permissible misalignment.

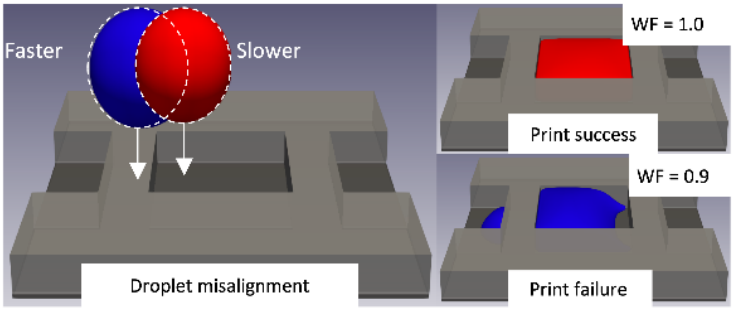

INTRODUCTION

Inkjet deposition is fast becoming utilised in many different disciplines, from the fabrication of wearable electronic devices[1], paper based flexible electronics[2], biomolecular arrays[3], thin-film transistors[4] and organic light emitting diode (OLED) displays. Inkjet printing is a method of emerging interest for the fabrication of OLEDs as it allows for direct deposition of the functional material. One of the key challenges of this technology is achieving a uniform particle deposition after the carrier liquid has evaporated, as particles agglomerate at the droplet periphery due to droplet pinning and internal flow (coffee-ring effect)[5]. Hence there is interest in mitigating this effect[6, 7]. As screen resolution increases, pixel size decreases, and as such the use of inkjet deposition would require highly accurate positioning of the printer head.

Printer head accuracy is usually in the range of 5-10μm, however, angular deflection of the droplet leaving the nozzle can cause greater misalignment of the droplet[8]. To ensure the droplets fall within the cavity, hydrophobic banked walls are usually used with a hydrophilic substrate. With increasing demand for increased resolution displays, smaller pixel sizes are needed. This makes ensuring a uniform droplet deposit more challenging. The aim of this research is therefore to investigate the limit of misalignment that still achieves a uniform deposit morphology inside a cavity.

The diameters of inkjet printed drops range from $10 - 100\mu m$, with velocities of $5 - 8m/s$. Dimensionless quantities related to inkjet printing are the Reynolds number, which is defined as $Re = UD/v$, where v is the kinematic viscosity and the Weber number, defined as $We = \rho U^2 D/\sigma$, where U is the droplet velocity, D is the droplet diameter and σ is the surface tension. Lower *We* numbers are preferable for a better control of the deposition morphology[9]. The Ohnesorge number is defined as $Oh = \sqrt{We}/Re$, with values ranging from ~0.1 < *Oh* <~1 considered to be suitable for printing[10].

One of the first numerical investigations into controlling droplets in (circular) cavities was by Khatavkar et al.[11], who used a diffuse interface model to investigate the effects of cavity wall thickness and contact angle on droplet confinement. It was found that a hydrophobic cavity wall enhances the confinement. Experiments with droplets of different Weber numbers were investigated for rectangular slots by Subramani et al.[12], where two splashing regimes were identified: one internal splash similar to impacts on planar surfaces and the other where the cavity structure causes a splash to extend outside of the cavity. Deposition into square cavities was investigated using a volume of fluid method by Yang et al.[13], including off-centre deposition, and it was found that the cavity did not fully fill for an off-centre deviation of $10\mu m$. Experiments and computational fluid dynamics (CFD) simulations of droplet deposition into cavities were performed by Liou et al.[14], where Weber number and cavity wall wettabilities were studied to find optimum wetting conditions. They reported that for a banked cavity wall there exists a critical contact angle of 70°, in which a uniform film is formed. Cavity configurations in terms of length to width ratios, Weber number and side wall contact angles were further investigated by Liou et al.[15]. They observed different morphologies for varying length to width ratios and subsequently reported how increases in We can enhance the cavity wetting. Other investigations into topographical alterations and wettabilities have been carried out with

the aim of enhancing the droplet positioning[16, 17]. Both utilised low contact angle substrates with walls of higher contact angle to confine the droplet, however it is reported for the rectangular cavity case that the wettabilities alone are not sufficient to enhance droplet spreading.

In this research, the popular mesoscale lattice Boltzmann method (LBM) was used. The method has widely reported amenability to run efficiently on parallel machines and graphical processing units[18, 19]. The LBM has been used to simulate a wide variety of problems, including single-phase high Reynolds number flows, multi-phase and multi-component flows such as droplet coalescence[20], evaporation and particle assembly[21]. The LBM has recently to the time of writing been used to study deposition into cavities for both single[22] and successive droplet deposition onto non-ideal wettability cavities[23].

Although previous research has elucidated the behavior of the deposition of single droplets into square and rectangular cavities, there is still a need to understand the behavior of droplet deposition under print-head misalignment and how non-uniform wettabilities affect the final equilibrium morphology. Previous works have focused on characterizing the behavior of fixed droplet sizes or the generation of multiple drops for a given cavity size, thus there is a requirement to understand the deposition of varying size droplets. This article investigates the deposition of a single droplet into square cavities with print-head misalignment. We examine properties such as cavity wettability, droplet size and level of droplet misalignment.

METHODOLOGY

The LBM is a mesoscale solver that comprises a two-step process of the streaming and collision of discrete particle distribution functions $f_i(x,t)$ referred to as populations. During the collision process, populations are relaxed towards a local Maxwellian equilibrium. Streaming populations involves moving them along discretised velocity paths to neighbouring nodes. The Bhatnagar–Gross–Krook [24] (BGK) collision operator was used where populations are relaxed with a single relaxation time τ. The LBM with the BGK collision operator is expressed as:

$$f_i(x+\vec{e}_i\Delta t, t+\Delta t) - f_i(x,t) = -\frac{f_i - f_i^{eq}}{\tau}\Delta t \qquad (1)$$

where *x* is a position in the lattice, $\vec{e_i}$ is a discrete lattice velocity, Δt is a time step, τ is the relaxation time and f_i^{eq} is the equilibrium distribution function, which is expressed as:

$$f_i^{eq} = w_i\rho\left(1 + \frac{\vec{u}\cdot\vec{e}_i}{c_s^2} + \frac{(\vec{u}\cdot\vec{e}_i)^2}{2c_s^4} - \frac{\vec{u}\cdot\vec{u}}{2c_s^2}\right) \qquad (2)$$

where ρ is the macroscopic density, $\vec{u}$ is the macroscopic velocity and c_s is the lattice speed of sound. The quantity w_i is the weighting coefficient for a specific velocity component. For this study the D3Q19 velocity set was used, which has weighting coefficients of $w_o = 1/3$, $w_{1-6} = 1/18$ and $w_{7-18} = 1/36$. The macroscopic quantities of density and velocity can be calculated as:

$$\rho(\boldsymbol{x},t)=\sum_i f_i(x,t), \quad \vec{u}(x,t)=\sum_i \vec{e}_i f_i(\boldsymbol{x},t)/\rho(\boldsymbol{x},t) \tag{3}$$

The multi-phase capability was incorporated via the Shan-Chen[25] model. The Shan-Chen multi-phase model introduces a force $\vec{F}$ between each node:

$$\vec{F}(x,t)=-G\psi(x,t)\sum_i w_i^{sc}\psi(x+\vec{e}_i\Delta t,t)\,\vec{e}_i \tag{4}$$

where *G* takes the form of a particle interaction potential strength parameter, which enables attractive forces with a negative value and repulsive forces for a positive. Specific weighting coefficients, w_i^{sc} are related to the discrete lattice velocity path. The magnitude of the force is determined by the values of ψ (pseudo-potential) at a node (x,t) and the value of a neighbouring nodes $(x+\vec{e}_i\Delta t,t)$. The pseudo-potential is a function of density taking the form:

$$\psi(\rho)=\rho_0[1-\exp(-\rho/\rho_0)] \tag{5}$$

where ρ_0 is a reference density, which was chosen to be unity for simplicity. As long as the interaction potential *G* is below the critical value of -4.0, the fluid is able to spontaneously separate into two phases, with heavy and light densities ρ_H and ρ_L respectively. The resulting non-ideal equation of state (EOS) with the modified model is expressed as:

$$p=\rho RT+\frac{GRT}{2}[\psi(\rho)]^2 \tag{6}$$

where $RT = 1$. However, different equations of state can be incorporated to achieve higher density ratios[26]. The Shan-Chen force is then incorporated into the model by shifting the velocity via:

$$\vec{u}(x,t)=\vec{u}(x,t)+\tau\vec{F}(x,t)/\rho(x,t) \tag{7}$$

Incorporating this interparticle force generates regions of high and low densities separated by a diffuse interface, which evolves naturally in a smooth manner during the simulation. The half-way bounce-back boundary condition was utilised for all the solid regions for no-slip. As the walls align with lattice nodes, the method is formally second order accurate, however, the true position of the no-slip wall is viscosity dependent and approximately $\Delta x/2$ lattice spacing from the solid node. The diffuse interface alleviates the need for any special treatment at no-slip boundaries to avoid singularities of the moving contact line. Open areas are periodic, which connects opposite ends of the domain in the streaming step. To control the contact angle at the solid surface, artificial density values are defined for the substrate and microstructure, denoted as $\rho_b$and ρ_m respectively. An analytical expression for the contact angle (assuming planar interfaces) is given by Benzi et al.[27] which was used for validation of our model, Figure 1. A number of simulations were performed, varying the substrate density ρ_b to determine the corresponding equilibrium contact angle. Droplets were initialised above a solid floor in a 61 × 61 × 61 domain with periodic boundaries along the sides. The density was varied from 0.1 to 1.8

in increments of 0.1 with the simulation running until the droplet reached a steady state, after which the height, *H* and diameter, *D* of the droplet were measured from the centre of the diffuse interface and used to calculate the contact angle as:

$$\theta = 2tan^{-1}\left(\frac{2H}{D}\right) \quad (8)$$

Excellent agreement is seen between the measured and predicted contact angles, particularly over the range of interest in this paper. The deviations at the extremes are attributed to curvature effects. For convenience, the results in Figure 1 are well fitted by the function $\theta = 177.2\exp(-0.959\rho_b)$, which is easily inverted to give the useful expression of ρ_b in terms of the desired contact angle:

$$\rho_b = 5.456 - 1.054\ln(\theta) \quad (9)$$

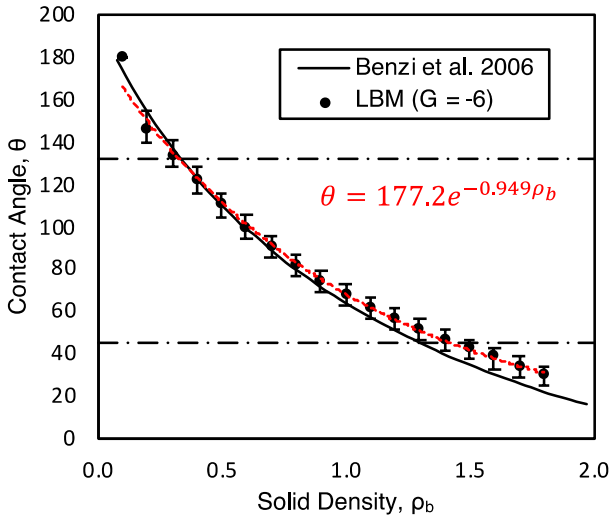

Figure 1: Contact angle as a function of wall density ρ_b. LBM results (•) plotted against analytical solution proposed by Benzi et al.[27]. Error bars represent measurement uncertainties of *D* and *H* due to diffuse interface of the method.

RESULTS AND DISCUSSION

To gain an understanding of the effects of print-head misalignment, simulations were configured to explore the effects of off-center droplet deposition. Although conventional print heads move along a single axis, the moving substrate introduces another potential source of misalignment, therefore parameters of overlap, *α*, are introduced for both the *x* and *z* axis, Figure 2. Overlap is a dimensionless quantity which determines how much of the droplet is initially positioned outside the cavity projected volume. For $\alpha = 0$ the full droplet will be initially positioned inside the projected cavity volume, for $\alpha = 1$ the full droplet is outside the projected cavity volume and for $\alpha = 0.5$ the droplet centre aligns with a cavity edge. All inputs to the simulation are in lattice units, therefore comparisons to real world cases are made via ensuring dimensionless parameters such as the Reynolds, Weber and Ohnesorge numbers match the ones typically observed in printing.

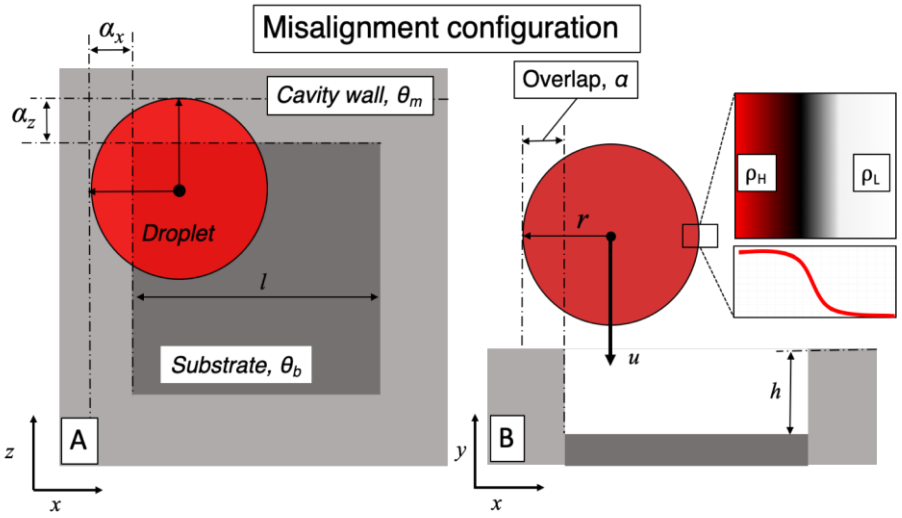

Figure 2: Configuration used in LBM simulations. Droplet with radius *r*, velocity *u* and density ρ_H surrounded by a light phase fluid of density ρ_L. Cavity with length *l*, height *h*, substrate contact angle θ_b cavity wall contact angle of θ_m. (A) Top projection view illustrating droplet overlap in a cavity corner by defining α_x and α_z as independent parameters. (B) Cross-sectional cut out view displaying the cavity in addition to an illustration of the diffuse interface between the droplet and surrounding fluid.

Unlike other LBM multiphase models[28], the surface tension is not an input value but rather is controlled by the interaction parameter, *G*. In the Shan-Chen multiphase model, *G* acts as a temperature-like parameter, responsible for the coexistence of heavy and light phases. To determine the surface tension, *σ*, the Young-Laplace relation was determined. This involves running several simulations with droplets of different diameters and recording the pressure both inside and outside of the droplet. The pressure difference Δp, is related to the inverse of the droplet radius, 1/*r*. The relation $\Delta p = 2\sigma/r$ then gives the surface tension, which for *G* = -6 is 0.154 in lattice units. The equilibrium density ratio for the given interaction strength is $\rho_H/\rho_L = 35$. The simulation is initialised with a density ratio of 41, as this improved simulation stability. The dynamic viscosity ratio is also 35, due to the relaxation time τ, set to 1 for both heavy and light phases.

The computational domain consists of 121 × 61 × 121 lattice nodes in the *x*, *y* and *z* axes respectively. The cavity area was set to be 45 × 45 lattice nodes with a height of 10 lattice nodes. The half-way bounce-back boundary condition was applied to all solid nodes defining the cavity as well as the roof of the simulation. As the droplet centre is initialised at a node and the true boundary location of the half-way bounce back method is approximately $\Delta x/2$ distance from the solid node, a slight underprediction of the overlap value is observed, such that for a droplet of *r* = 15 initialised above a solid wall with an apparent overlap of 0.5, i.e. half the droplet is initially located outside the cavity, the true value would be 0.516 due to the additional ½ lattice spacing. As the difference between these values is less than 4% for the droplet sizes of interest to this study the apparent overlap value is used henceforth. The open boundaries at the edge of the computational domain were set as periodic. The substrate and cavity microstructure contact angles θ_b and θ_m respectively were controlled independently by setting an effective density value to the solid nodes via equation 9. In each of the simulations a wetted fraction (*WF*) is

defined to determine the quality of the droplet deposition. The function observes nodes above the solid surface within the cavity and determines from the local density value if it is liquid or vapour, formally expressed in equation 10.

$$WF = \frac{1}{MN}\sum_{i=1}^{M}\sum_{j=1}^{N} H(\rho_{ij1} - \rho_c) \qquad (10)$$

M is the number of nodes in the *x* direction inside the cavity, *N* is the number of nodes in the *z* direction within the cavity, *H* is the Heaviside function and ρ_c is the critical value of the density set to $\rho_c = 10\rho_L$.

Single and Multiple-Axis Misalignment

In order to compare the conditions of single and multiple wall overlap, simulations were configured to match the ratio of the droplet volume initially located outside of the cavity wall projection, referred to as volume fraction (*VF*). The *VF* can be expressed in terms of overlap by $VF = 3\alpha^2 - 2\alpha^3$. Figure 3 displays the relationship between *α* and the *VF*. For simplicity in comparing results, the multiple wall case was set with overlap values of $\alpha_x = \alpha_z = 0.5$, which results in *VF* = 0.75, Figure 3 (a). The overlap of the droplet with a single wall, which results in a *VF* = 0.75 is found to be $\alpha_x = 0.674$. A droplet diameter of 34 and a starting position of $N_x = 32$ gives an offset value of $\alpha_x = 0.677$, Figure 3 (b), which is within a 1% error of the target value.

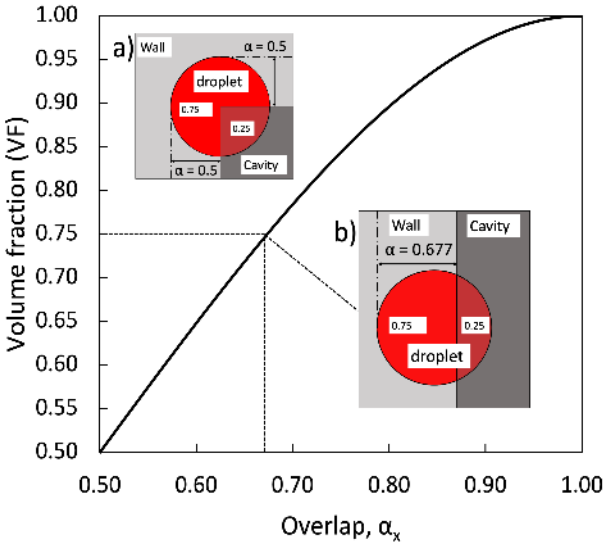

Figure 3: Solid line displaying the relation of the droplet volume located outside a single cavity wall at initialisation (*t* = 0) for a given overlap value α_x. Illustration of single wall overlap case where 0.75 of the droplet volume is initially located outside the cavity.

The droplets were initialised with a *y*-component velocity of -0.15 and a diameter of 34, which gives the dimensionless characteristics of *We* = 13.7, *Re* = 30.6 and *Oh* = 0.12. This speed is less than the 0.2 recommended[29] maximum speed to ensure that the simulations are conducted within the quasi-incompressible limit of the LB method. To verify that compressibility errors do not affect the results, a selection of simulations were

repeated with larger lattice resolutions, in which the droplet speed required to achieve the same *We* value was reduced to 0.106. No effect on the predictions was discernible as later indicated in Figure 6. The substrate and cavity wall contact angles were set to be 89°. Depositing the droplet over a corner of the cavity resulted in *WF* = 0.89, whereas deposition over a single wall resulted in a *WF* = 0.78, a 12.4% reduction. As common in characterizing the behavior of droplets[30], the evolution of the wetted fraction is recorded against dimensionless time *t** in Figure 4. The evolution of the *WF* exhibits similar behavior for both single and multiple axis overlap configurations. In each, there is a sharp increase in the *WF* until an initial peak value is reached in the inertial spreading regime, which is greater for the single wall case. After which the droplets recoil before beginning to wet the cavity under the influence of capillary force. The dimensionless time *t** is given by $t^* = tU/D$, where *t* is the time in lattice units, *U* is the initial velocity of the droplet, and *D* is the droplet diameter.

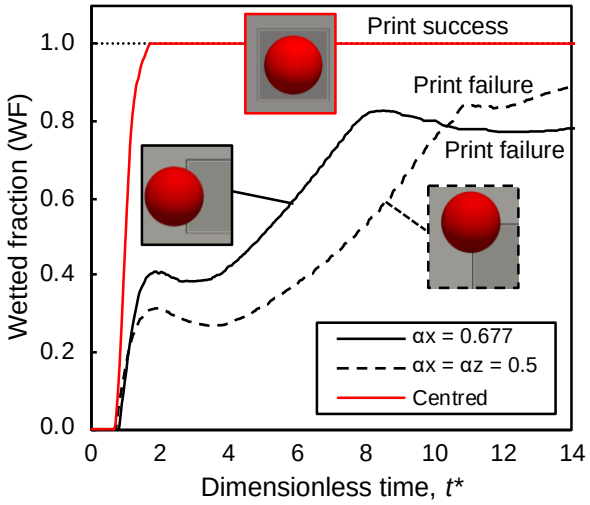

Figure 4: Dynamic evolution of cavity wetted fraction (*WF*) where θ_b = θ_m = 89°. Droplet properties of *Re* = 30.6, *We* = 13.17 *Oh* = 0.12. Droplets located with no overlap (solid red line), overlap over wall (solid black line) and a corner (dashed black line), both with 0.75 volume fraction located outside cavity at initialisation (*t* = 0). Overlap over wall value of α_x= 0.677 and a droplet impacting a cavity corner with overlap values of α_x = α_z = 0.5.

Substrate and Cavity Wall Wettabilities

The influence of substrate and cavity wall wettabilities is investigated by varying the two contact angles independently. The solid density value of the substrate and microstructure was varied from 0.3 to 1.5, which corresponds to contact angles of $132 - 45°$. In order to determine which conditions best mitigate against printer head misalignment, the droplets were initialised with an overlap value of $\alpha_x = 0.5$, and the wetted fraction was recorded at the end of each simulation, Figure 5, where dark blue regions are used to illustrate regions of high *WF*.

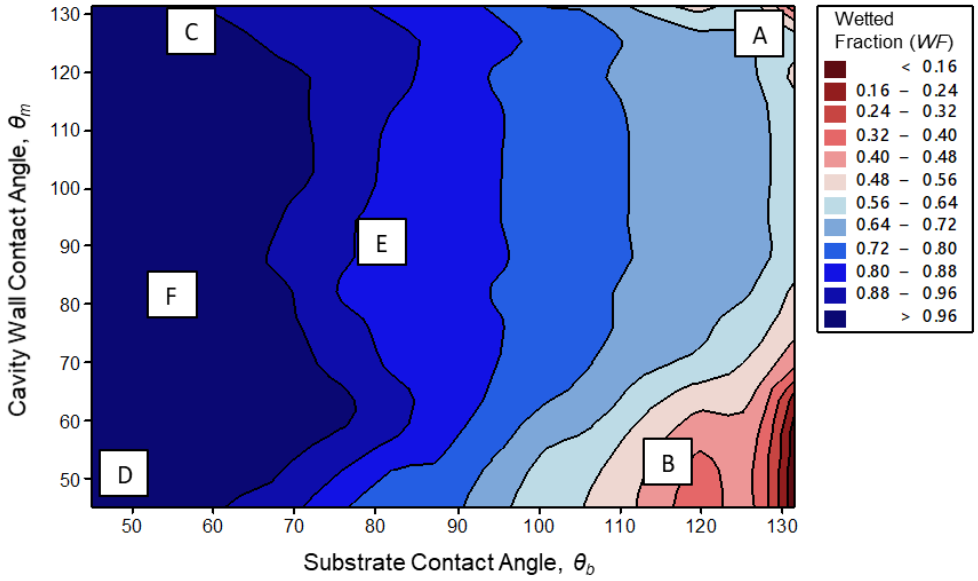

Figure 5: Colour contour plot for wetted fraction with varying substrate θ_b and cavity wall contact angle θ_m independently. Droplet properties of *Re* = 30.6, *We* = 13.17 *Oh* = 0.12 all initialised with overlap α_x= 0.5. Wetted fraction graded by high values (blue) to low values (red). Regions of different equilibrium morphologies A→F are highlighted and illustrated in Figure 6.

Points (A→F) on the contour plot have been chosen to illustrate the final droplet morphology. The hydrophilicity of the substrate has a strong influence on the final wetted fraction, with lower contact angles enhancing droplet spreading due to increased capillary forces. The wettability of the cavity wall, however, has a preferable window for optimum cavity wetting. The more hydrophilic the cavity wall is, the more likely the droplet is pinned outside the cavity, which is illustrated in Figure 6 (B) and (D). The value of this critical wall contact angle depends on the wettability of the substrate. For the cases where the cavity wall reaches its peak hydrophobicity, the droplet can be repelled from filling the cavity corners, Figure 6 (C). In the case where both the cavity wall and the substrate are at peak hydrophobicity, the droplet falls within the cavity and is fully confined by the cavity walls, but no spreading occurs, Figure 6 (A). If the cavity wall is hydrophilic and the substrate is hydrophobic, the majority of the droplet becomes pinned outside the cavity, Figure 6 (B), which results in a low wetted fraction of *WF* = 0.27. Given a hydrophilic substrate with a contact angle of $\theta_b = 45°$ a wettability difference for the microstructure of $\theta_m \geq \theta_b + 12°$ was found to fully draw the droplet into the cavity without any external wetting, Figure 6 (F).

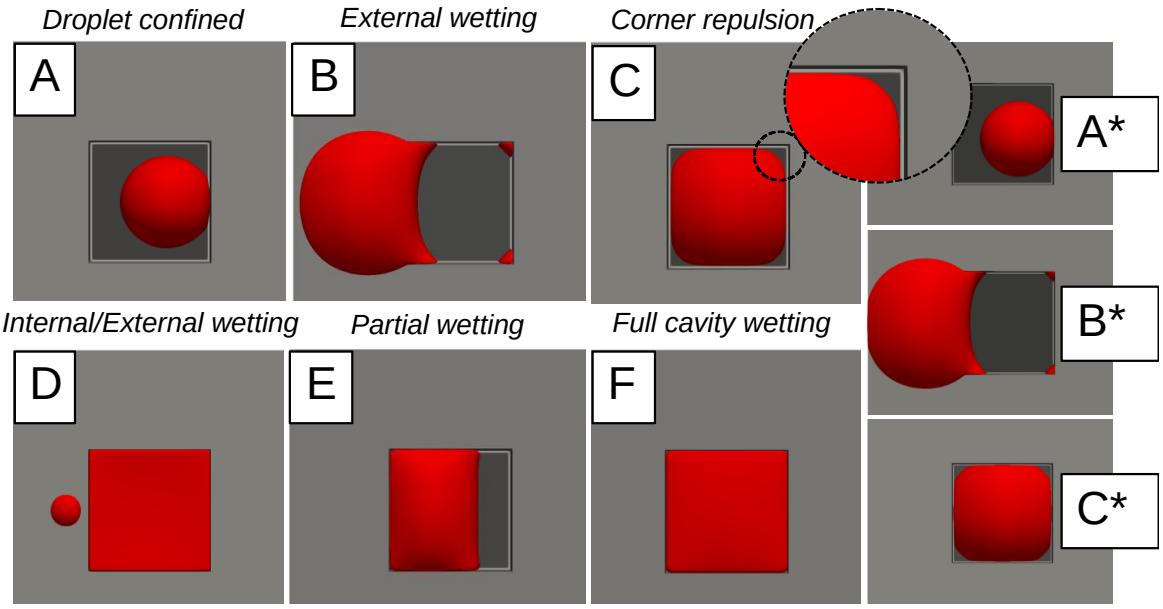

Figure 6: Droplet formations for varying substrate and cavity wall contact angles. Darker regions within the cavity illustrate lower contact angles. Substrate and cavity wall at peak hydrophobicity (A) θ_b = 132° and θ_m = 132°. Hydrophilic cavity wall and hydrophobic substrate (B) θ_b = 115° and θ_m = 49°. Hydrophobic wall and hydrophilic substrate (C) θ_b = 64° and θ_m = 132°. Hydrophilic wall and substrate (D) θ_b = 49° and θ_m = 49°. Hydrophilic wall and substrate (E) θ_b = 92° and θ_m = 82°. Hydrophilic wall and substrate (F) θ_b = 64° and θ_m = 82°. Figures marked with an asterisk are performed with a doubled lattice density (i.e. 242 × 122 × 242) to verify grid independence.

The results from Figure 5 also show uniform fully wetted droplet deposition for specific cases of equal substrate and cavity microstructure wettabilities. Fully wetted cavities were achieved with equal substrate and microstructure contact angles in the range of $73 \rightarrow 45°$, however there were parts of the droplet pinned outside the cavity for the lower contact angles ($\theta < 58°$). For the uniform hydrophilic substrate and cavity wall microstructure within the contact angle range of $73 \rightarrow 58°$ the droplet fully wets the cavity and is also fully confined. Investigating these parameters further, simulations were performed with increasing levels of single wall overlap for uniform wettabilities of 58, 64, and 74°, in which it was found that the uniform wettability cavity of 64° resulted in the largest value of permissible overlap, $\alpha_{max} = 0.706$, that still fully fills the cavity in the available time. The rate at which the cavity fills is illustrated for uniform and non-uniform cavities in Figure 7. Both cases display a linear rate of wetting after the initial impact region, however, the non-uniform case exhibits a quicker wetting rate.

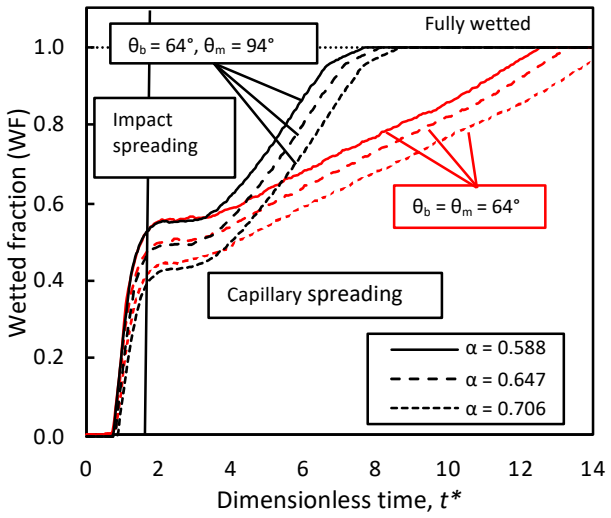

Figure 7: Evolution of wetted fraction for uniform cavity wettability $\theta_b = \theta_m = 64°$ (red lines) and non-uniform wettability $\theta_b = 64°$ and $\theta_m = 94°$ (black lines). Overlap values represented by $\alpha_x = 0.588$ (solid lines), $\alpha_x = 0.647$ (dashed lines) and $\alpha_x = 0.706$ (dotted lines). Droplet properties of *Re* = 30.6, *We* = 13.17 *Oh* = 0.12.

Filling Time and Limit to Droplet Misalignment

In this section the limit of single axis overlap keeping all dimensionless numbers constant is investigated for two non-uniform cavity wettabilities with different wettability ratios. The overlap is increased and the time, *t** at which the cavity is fully wetted is recorded, Figure 8. There is an approximate linear relationship between the level of overlap and the time taken to fill the cavity displayed for both ratios, with an increased value resulting in a quicker filling time.

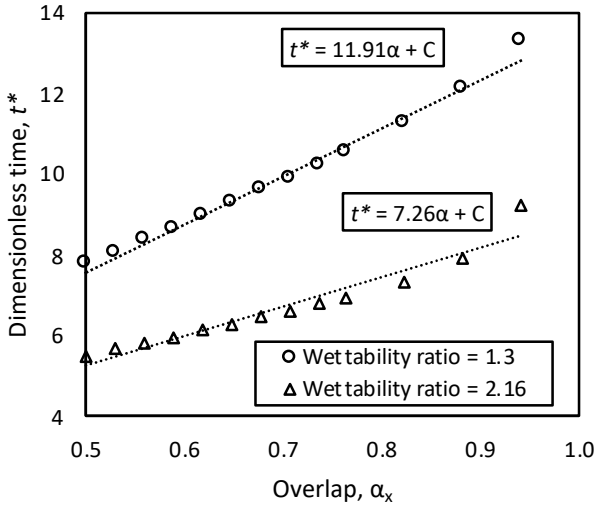

Figure 8: Dimensionless time *t** taken to fully wet the cavity as a function of overlap $\alpha_x = 0.5 \rightarrow 0.981$. Cavity properties $\theta_b = 64°$ and $\theta_m = 83°$. Droplet properties of *Re* = 51, *We* = 36.58 *Oh* = 0.12.

Filling Cavities with Varying Droplet Sizes

The cases where the droplet fully fills the cavity in the range where it is fully confined is useful in controlling the deposited material thickness with a single drop, as there is a practical limit to volume fraction of material within printable fluids. Different size droplets were generated to investigate the effects of filling a cavity with and without droplet overlap. The cavity wettabilities were set to enhance filling with the substrate contact angle $\theta_b = 64°$ and cavity wall wettability set to $\theta_m = 83°$. Droplet diameters of 20, 24, 26, 28, 32, 34, 36, 40, 44 and 50 were implemented both in the centre of the cavity and with an overlap value of α_x = 0.5. The final wetted fraction was plotted against the droplet diameter divided by the cavity length. The ratio of *D/l* indicates the critical values at which a cavity is filled for droplets with and without overlap. For a centred droplet the critical filling *D/l* value for the given substrate conditions was 0.62, whereas for a droplet with overlap $\alpha_x = 0.5$ the critical *D/l* value was 0.76. The increased value is attributed to droplets' inability to spread evenly along the cavity once misaligned. For the smallest tested droplet diameter *D* = 20, the case in which the droplet was misaligned resulted in a higher wetted fraction, which is attributed to evaporation of the centred droplet. Subsequent increase in the droplet diameter resulted in higher wetted fraction for both droplet positions, Figure 9.

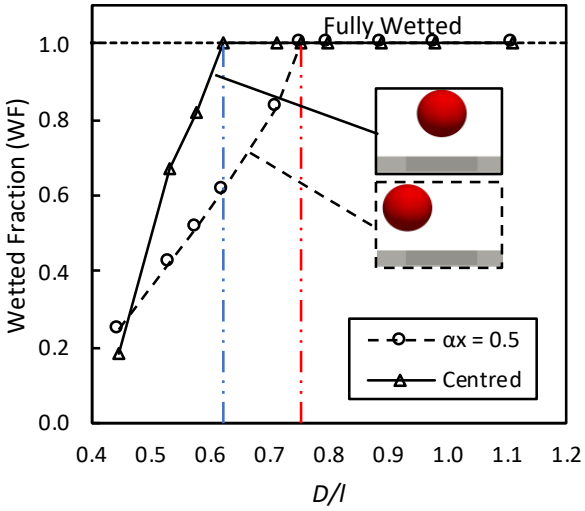

Figure 9: Final wetted fraction at $t^* = t^*_{max}$ for droplets of varying diameter, *D* deposited at the cavity centre (black line) and droplets positioned with overlap α_x = 0.5 (dashed line). Cavity properties θ_b = 64° and θ_m = 83°.

Limit of Droplet Misalignment for Cavities in Close Proximity

As cavities are in close proximity to one another when for example forming a pixel, the single cavity domain was modified to incorporate neighbouring cavities. Therefore, the limits in droplet misalignment without contaminating another cavity can be explored, Figure 10. This was achieved by adding additional cutouts either side of the cavity, which have length equal to $l/2$ from the sides of the simulation domain, such that through the periodic boundary condition a complete cavity is formed. The addition of another cavity creates a separating wall, with thickness *w*. Given preferential non-uniform wettabilities of the cavity, investigations into single wall overlap was performed for α_x = 0.618. With

the modified domain the droplet impacts the cavity wall and spreads over both sides, the droplet is able to remain fully intact and due to the centre cavity becoming initially wetted, the droplet is drawn in and is fully confined, Figure 10 (a). When the wall thickness is reduced, the droplet spreads sufficiently over both sides of the wall to connect with the hydrophilic substrate causing the droplet to split into two, Figure 10 (b). Reducing the speed of the droplet mitigates against the spreading over the left-hand side of the cavity wall, and results in successful deposition, Figure 10 (c). The size of the wall is a key factor limiting the maximum overlap.

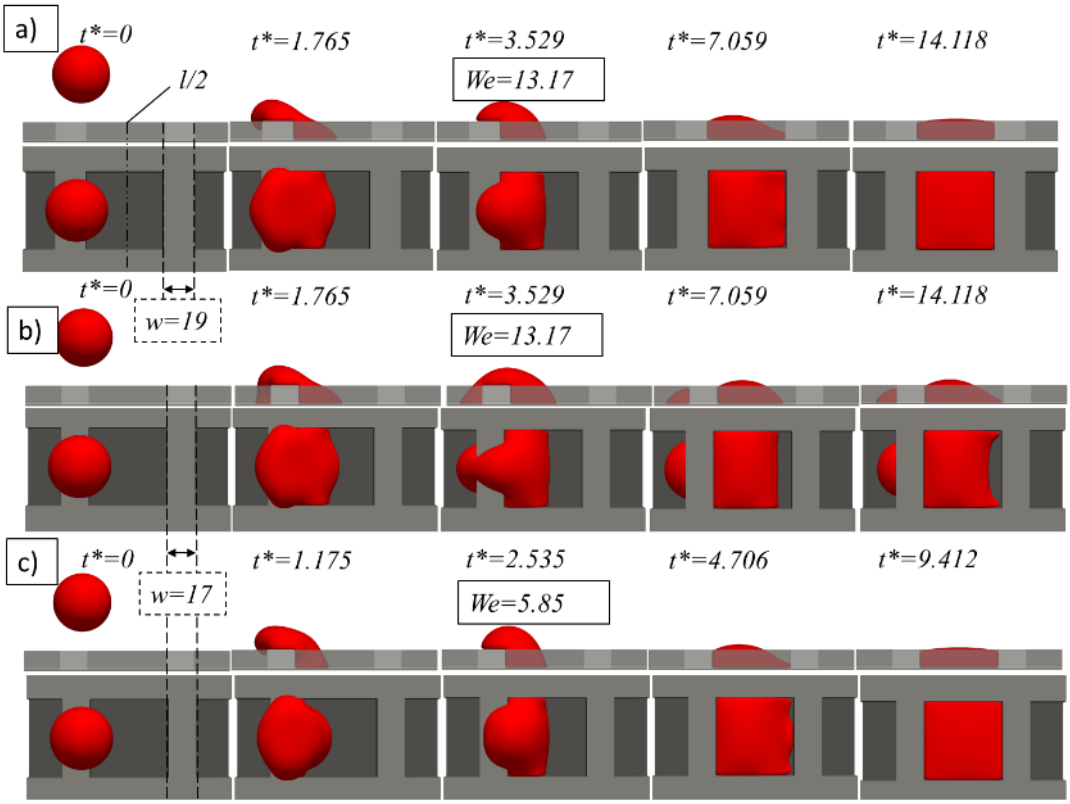

Figure 10: Droplet with α_x = 0.6176, *Re* = 30.6, *We* = 13.17 *Oh* = 0.12, impacting a cavity wall with of thickness 19 (a), cavity wall with thickness 17 (b) and cavity wall with thickness 17 with *Re* = 20.4, *We* = 5.85 *Oh* = 0.12. Cavity properties θ_b = 64° and θ_m = 83°(c).

The final wetted fraction for (b) was *WF* = 0.898, whereas (a) and (c) resulted in *WF* = 1. Given a multiple cavity configuration, the maximum achievable overlap is limited by the wall thickness, droplet diameter and the wall height, *h*. Printing can be improved by reducing the initial droplet speed as in (c). For cases where the wall thickness is equal to the droplet radius a maximum overlap value of α_{max} = 0.618 was achievable. In order to relate the dimensionless quantities of the simulations to physical print-head position tolerances, a parameter (*P*) is introduced to account for the maximum allowable misalignment for a cavity of a given size and wetting characteristics. The following expression can be used to give the maximum positional error for a given α_{max} as:

$$\frac{P}{l} = \frac{1}{2} + \left(\alpha_{max} - \frac{1}{2}\right)\frac{D}{l} \tag{11}$$

This equation gives a parameter space in which a droplet can be successfully deposited into a cavity and is plotted in Figure 11. The equation holds for situations where the droplet is of sufficient size to fill the cavity. Note that the gradient of the line in Figure 11 is dependent on the wetting characteristics of the cavity substrate and microstructure.

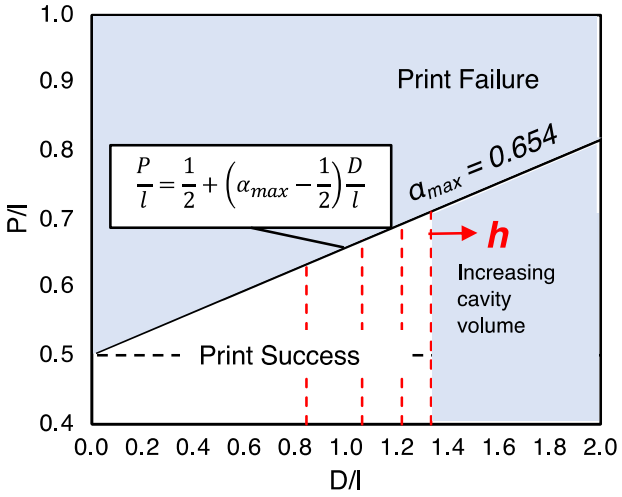

Figure 11: Printing parameter space based on Equation 11. Unshaded region showing areas of print success. Printable area can be increased by an increases value of α_{max} and *D/l*.

CONCLUSIONS

In this work the pseudopotential lattice Boltzmann method was used to investigate the effects of print-head misalignment on the equilibrium morphology of the droplets deposited into square cavities. First looking at single vs multiple axis misalignment, it was found that when the droplet impacts a cavity corner a higher wetted fraction would result. The magnitude of print-head misalignment is quantified by the fraction of the droplet initially located outside of the cavity wall, referred to as overlap (α). Simulations were performed with varying wettabilities of the cavity microstructure and substrate, which revealed 6 distinct equilibrium conditions. The results also highlighted cases of uniform cavity wettabilities in which the cavity would be successfully filled. These uniform wettability cavities were then used to determine the maximum achievable misalignment in terms of α_{max}. For a cavity of uniform wettability of 64° a maximum overlap value of $\alpha_{max} = 0.647$ was found. For non-uniform wettability cavities with $\theta_b = 45°$ for wall and $\theta_m = 60°$ the maximum overlap was found to be $\alpha_{max} > 0.9$. We then looked into the effects of droplet size where the droplet diameter was normalized by the cavity length to give the ratio at which the cavity would become filled. Finally, the effects of closely positioned cavities on deposition under misalignment was explored where it was found that the presence of another cavity reduces the achievable α_{max} as contamination with neighbouring cavities becomes apparent. All parameters were then combined into a single equation to give the printing parameter space which results in successful deposition.

AUTHOR INFORMATION

Corresponding Authors

†Email: mnffj@leeds.ac.uk

†Email: k.kubiak@leeds.ac.uk

Notes

The authors declare no competing financial interest.

AKNOWLEDGMENTS

The authors are grateful to the UK Consortium on Mesoscale Engineering Sciences (UKCOMES) (Grant No. EP/L00030X/1 and EP/R029598/1), and K.J.K. is grateful for the support from EP/P022243/1. The authors also thank the University of Leeds and the University of Huddersfield (EPSRC-DTP EP/R513234/1) for the funding. M.M. is grateful for support from EP/R010366/1.

REFERENCES

(1) Gao, M. *et al.*, Inkjet printing wearable electronic devices. *Journal of Materials Chemistry C* **2017,** *5*, 2971-2993.
(2) Wang, Y. *et al.*, Paper-Based Inkjet-Printed Flexible Electronic Circuits. *ACS Applied Materials & Interfaces* **2016,** *8*, 26112-26118.
(3) Zaugg, F. G.; Wagner, P., Drop-on-Demand Printing of Protein Biochip Arrays. *MRS Bull.* **2003,** *28*, 837-842.
(4) Sirringhaus, H. *et al.*, High-resolution inkjet printing of all-polymer transistor circuits. *Science* **2000,** *290*, 2123-2126.
(5) Deegan, R. D. *et al.*, Capillary flow as the cause of ring stains from dried liquid drops. *Nature* **1997,** *389*, 827.
(6) Anyfantakis, M. *et al.*, Modulation of the Coffee-Ring Effect in Particle/Surfactant Mixtures: the Importance of Particle–Interface Interactions. *Langmuir* **2015,** *31*, 4113-4120.
(7) de Gans, B.-J.; Schubert, U. S., Inkjet Printing of Well-Defined Polymer Dots and Arrays. *Langmuir* **2004,** *20*, 7789-7793.
(8) Geffroy, B. *et al.*, Organic light-emitting diode (OLED) technology: materials, devices and display technologies. *Polym. Int.* **2006,** *55*, 572-582.
(9) Yang, X. *et al.*, Oscillation and Recoil of Single and Consecutively Printed Droplets. *Langmuir* **2013,** *29*, 2185-2192.
(10) Hoath, S. D., *Fundamentals of Inkjet Printing: The Science of Inkjet and Droplets*. Wiley-VCH: DE, 2016.
(11) Khatavkar, V. V. *et al.*, Diffuse interface modeling of droplet impact on a pre-patterned solid surface. *Macromol. Rapid Commun.* **2005,** *26*, 298-303.
(12) Subramani, H. J. *et al.*, Dynamics of Drop Impact on a Rectangular Slot. *Industrial & Engineering Chemistry Research* **2007,** *46*, 6105-6112.

(13) Yang, A. *et al.*, Numerical study for the impact of liquid droplets on solid surfaces. *Proceedings of the Institution of Mechanical Engineers, Part C: Journal of Mechanical Engineering Science* **2007,** *221*, 293-301.
(14) Liou, T. *et al.*, Effects of Impact Inertia and Surface Characteristics on Deposited Polymer Droplets in Microcavities. *Journal of Microelectromechanical Systems* **2008,** *17*, 278-287.
(15) Liou, T.-M. *et al.*, Study of the characteristics of polymer droplet deposition in fabricated rectangular microcavities. *Journal of Micromechanics and Microengineering* **2009,** *19*, 065028.
(16) Kant, P. *et al.*, Sequential deposition of microdroplets on patterned surfaces. *Soft Matter* **2018**.
(17) Suh, Y.; Son, G., Numerical Simulation of Droplet Deposition and Self-Alignment on a Microstructured Surface. *Numerical Heat Transfer, Part A: Applications* **2010,** *57*, 415-430.
(18) Huang, T.-C. *et al.*, Simulation of droplet dynamic with high density ratio two-phase lattice Boltzmann model on multi-GPU cluster. *Computers & Fluids* **2018,** *173*, 80-87.
(19) Çelik, S. B. *et al.* In *Simulation of lid-driven cavity flow by parallel implementation of lattice Boltzmann method on GPUs*, International Symposium on Computing in Science and Engineering (ISCSE 2011), 2011.
(20) Castrejon-Pita, J. R. *et al.*, The dynamics of the impact and coalescence of droplets on a solid surface. *Biomicrofluidics* **2011,** *5*, 014112-014112.
(21) Zhao, M.; Yong, X., Modeling Evaporation and Particle Assembly in Colloidal Droplets. *Langmuir* **2017,** *33*, 5734-5744.
(22) Zhang, L. *et al.*, Inkjet droplet deposition dynamics into square microcavities for OLEDs manufacturing. *Microfluid. Nanofluid.* **2018,** *22*, 47.
(23) Zhang, L. *et al.*, Lattice Boltzmann study of successive droplets impingement on the non-ideal recessed microchannel for high-resolution features. *Int. J. Heat Mass Transfer* **2018,** *120*, 1085-1100.
(24) Bhatnagar, P. L. *et al.*, A model for collision processes in gases. I. Small amplitude processes in charged and neutral one-component systems. *Phys. Rev. A* **1954,** *94*, 511.
(25) Shan, X.; Chen, H., Lattice Boltzmann model for simulating flows with multiple phases and components. *Physical Review E* **1993,** *47*, 1815-1815.
(26) Yuan, P.; Schaefer, L., Equations of state in a lattice Boltzmann model. *Phys. Fluids* **2006,** *18*, 042101.
(27) Benzi, R. *et al.*, Mesoscopic modeling of a two-phase flow in the presence of boundaries: The contact angle. *Physical Review E* **2006,** *74*, 021509.
(28) Swift, M. R. *et al.*, Lattice Boltzmann Simulation of Nonideal Fluids. *Phys. Rev. Lett.* **1995,** *75*, 830-833.
(29) Krüger, T., *The Lattice Boltzmann method: principles and practice*. Springer: 2017.
(30) Rioboo, R. *et al.*, Time evolution of liquid drop impact onto solid, dry surfaces. *Exp. Fluids* **2002,** *33*, 112-124.